

# Crystallization of Coccolith Calcite at Different Life-Cycle Phases Exhibits Distinct Degrees of Cellular Confinement

Oz Ben-Joseph, Diede de Haan, Katya Rechav, Eyal Shimoni, Smadar Levin-Zaidman, Gerald Langer, Ian Probert, Glen L. Wheeler, and Assaf Gal\*

Coccolithophores are a group of unicellular marine algae that shape global geochemical cycles via the production of calcium carbonate crystals. Interestingly, different life-cycle phases of the same coccolithophore species produce very different calcitic scales, called coccoliths. In the widely studied diploid phase, the crystals have anisotropic and complex morphologies, while haploid cells produce coccoliths consisting solely of calcite crystals with simple rhombohedral morphology. Understanding how these two life-cycle phases control crystallization is a highly sought-after goal, yet, haploid phase crystallization has rarely been studied, and the process by which they form is unknown. Herein, advanced electron microscopy is employed to elucidate the cellular architecture of the calcification process in haploid cells. The results show that in contrast to diploid-phase calcification, the coccolith-forming vesicle of haploid-phase cells is voluminous. In this solution-like environment, the crystals nucleate and grow asynchronously in a process that resembles calcite growth in bulk solution, leading to the simple morphologies of the crystals. The two distinct mineralization regimes of coccolithophore life-cycle phases suggest that cellular architecture, and specifically confinement of the crystallization process, is a pivotal determinant of biomineral morphology and assembly.

## 1. Introduction

Biomineralization pathways exercise high levels of control over crystallization reactions, capable of producing single crystals with intricate shapes that are rare at geological and synthetic settings.<sup>[1,2]</sup> To form these complex crystals, the formation environment of biominerals is usually within confined spaces where the chemical and spatial conditions are highly regulated by cells.<sup>[3–5]</sup> However, the factors that direct crystal growth to result in such unique morphologies are poorly understood and are of great interest to biomineralization and materials science.<sup>[6,7]</sup>

One of the most intriguing examples of biologically controlled crystal morphology is the calcite elements produced by unicellular marine algae called coccolithophores.<sup>[8]</sup> These mineralized elements, termed coccoliths, are composed of an array of complex and anisotropic crystal morphologies that are species-specific.<sup>[9,10]</sup>

Interestingly, the regulation over calcite crystal morphology fundamentally differs between the two life-cycle stages of a single coccolithophore species.<sup>[11,12]</sup> In contrast to the elaborate crystals produced at the diploid stage, called heterococcoliths, the crystal morphology in coccoliths of the haploid stage, termed holococcoliths, is solely rhombohedral,<sup>[8]</sup> the most common morphology of calcite.

The biomineralization pathway of the complex heterococcolith crystals has been the focus of numerous studies that have elucidated the role of cellular structures involved in the crystallization process.<sup>[9,13–16]</sup> Crystallization takes place intracellularly within the confined environment of a membrane-bound organelle termed the coccolith vesicle.<sup>[3,16]</sup> The first structure to form is an organic base plate scale, which serves as a template for crystal nucleation.<sup>[9,17]</sup> Calcite nucleation takes place simultaneously at defined locations and orientations around the base plate periphery, forming a ring of simple rhombohedral crystals.<sup>[8,18]</sup> Subsequently, anisotropic crystal growth occurs within the vesicle, ultimately forming the intricate morphologies characteristic of the fully developed heterococcolith crystals.<sup>[10,19]</sup>


Heterococcolith formation is tightly linked to highly acidic soluble macromolecules, termed coccolith-associated polysaccharides (CAPs).<sup>[20,21]</sup> CAPs are found during coccolith development in complexes with  $\text{Ca}^{2+}$  ions, and as a coating material over

O. Ben-Joseph, D. de Haan, A. Gal  
Department of Plant and Environmental Sciences  
Weizmann Institute of Science  
Rehovot 7610001, Israel  
E-mail: assaf.gal@weizmann.ac.il

K. Rechav, E. Shimoni, S. Levin-Zaidman  
Department of Chemical Research Support  
Weizmann Institute of Science  
Rehovot 7610001, Israel

G. Langer, G. L. Wheeler  
The Laboratory  
Marine Biological Association  
Citadel Hill, Plymouth PL1 2PB, UK

I. Probert  
FR2424 Sorbonne University/CNRS  
Station Biologique de Roscoff  
29680 Roscoff, France

 The ORCID identification number(s) for the author(s) of this article can be found under <https://doi.org/10.1002/sstr.202200353>.

© 2022 The Authors. Small Structures published by Wiley-VCH GmbH. This is an open access article under the terms of the Creative Commons Attribution License, which permits use, distribution and reproduction in any medium, provided the original work is properly cited.

DOI: 10.1002/sstr.202200353

the mature crystals. These macromolecules were suggested not only to transport  $\text{Ca}^{2+}$  into the calcification environment but also to promote altered crystal morphologies by forming stereochemical interactions with the growing crystals.<sup>[22,23]</sup> However, recent work shows that developing heterococcolith crystals present only the rhombohedral crystal facets, ruling out growth modification by such stereochemical means.<sup>[10]</sup>

The understanding of holococcolith formation severely lags behind that of heterococcoliths, with only a handful of investigations to date,<sup>[24–27]</sup> which all report on conserved holococcolith architectures that point to a highly regulated biomineralization process. The difficulty of culturing calcifying haploid cells was a major obstacle,<sup>[28]</sup> and only recently holococcolith formation was shown to be an intracellular process.<sup>[27]</sup> One of the most intriguing aspects is the fundamental differences in the crystallization processes, which lead to such distinct crystalline products in the two genetically identical cell types.

Here, we use advanced techniques of sample preparation, transmission electron microscopy (TEM), and 3D focused ion beam scanning electron microscopy (FIB-SEM) to investigate the cellular characteristics of the holococcolith formation pathway. We show that, as for heterococcoliths, holococcolith formation takes place within vesicles derived from the Golgi apparatus. However, holococcolith crystal nucleation does not depend on an organic scale, and crystal growth occurs in a voluminous liquid environment.

## 2. Results

### 2.1. Cellular Architecture and Holococcolith Morphology

We chose to study two coccolithophore species, *Calyptrosphaera* sp. and *Coccolithus braarudii*, available as haploid holococcolith-forming cultures. The two species are both members of the *Coccolithales* order but produce distinct holococcolith morphotypes, providing the opportunity to explore general traits of holococcolith formation. Both species exhibit sufficient growth in laboratory conditions (Figure S1, Supporting Information), and a full coccolith coverage of the cells is present throughout culture growth (Figure 1). The holococcolith morphology of *C. braarudii* is a flat ellipse with a double layer of crystals, situated one on top of the other, delimiting the periphery of an organic base plate, while the center can be fully or partially covered by a monolayer of crystals (Figure 1c). The holococcoliths produced by *Calyptrosphaera* sp. are of a hollow sphere-like shape, where only a subset of the crystals is in contact with the organic base plate (Figure 1d).

To study the structural aspects of holococcolith producing cells, we prepared samples of exponential stage cultures for TEM analysis. The cellular environment was preserved using high-pressure freezing (HPF),<sup>[29]</sup> followed by freeze substitution and resin embedding.<sup>[30]</sup> In this method, a dense cell pellet is pressurized and immobilized at the temperature of liquid nitrogen to prevent the formation of destructive ice crystals. The sample is then chemically fixed and dehydrated during freeze substitution as it is slowly brought back to room temperature, thereby preserving cellular ultrastructure close to its native state. Ultrathin sectioning of resin-embedded samples was conducted

under anhydrous conditions to prevent the dissolution of holococcolith crystals. TEM images show the major intracellular organelles of the coccolithophore cell, including chloroplasts with a central pyrenoid, a nucleus, vacuoles, and cytoplasm, alongside the extracellular region (Figure 2). The vacuolar content in both strains is thin and lightly stained (Figure 2a,d), similar to the morphology of vacuoles in diploid coccolithophore cells.<sup>[31]</sup> However, we did not observe the characteristic dense phases embedded within.<sup>[32]</sup> Mature holococcoliths are found in the extracellular region, situated proximal to an outermost thin envelope layer (Figure S2, Supporting Information),<sup>[25]</sup> and distal to several layers of unmineralized scales and fibers (Figure 2c,f, S2, Supporting Information).

As crystal morphology is very different between heterococcoliths and holococcoliths, we investigated whether holococcolith crystals possess a coating of CAPs similar to that of heterococcoliths. We used a chemical fixation method for TEM, which was previously used to visualize the organic coat of heterococcolith crystals.<sup>[20,33]</sup> In this preparation, acidic conditions during the fixation stages result in complete dissolution of the coccolith calcite crystals, leaving the organic coating as a stained remnant of the crystal. Rhombohedral outlines were identified in the extracellular region of *Calyptrosphaera* sp., delimiting the shapes of the holococcolith crystals, indicating an organic coating over each calcite rhombohedron (Figure S3, Supporting Information). In addition, *Calyptrosphaera* sp. coccoliths interact with Ruthenium red, a positively charged dye forming specific interactions with uronic acid residues, indicating their presence in the coating material (Figure S3, Supporting Information). However, it is unclear whether a crystal coating is also present in *C. braarudii* because it could not be identified with this chemical fixation method and is not stained by Ruthenium red (Figure S3, Supporting Information).

### 2.2. Holococcolith Formation Process

In order to increase the possibility of observing developing holococcoliths in TEM preparations, we decalcified cells to remove extracellular coccoliths by acidifying their seawater medium. Restoring the pH to ambient levels induced intense recalcification and increased the fraction of actively calcifying cells in the culture (Figure S1, Supporting Information). Samples for TEM investigations of recalcifying cells were prepared using the same technique as for fully calcified cells (Figure 2). In this manner, we obtained a large TEM dataset of developing intracellular holococcoliths from both *Calyptrosphaera* sp. ( $n = 43$ ) and *C. braarudii* ( $n = 13$ ). In addition, 3D data of the calcification environment were acquired by a FIB-SEM slice-and-view workflow, altogether providing a detailed characterization of the holococcolith biomineralization pathway.

The images of calcifying cells show that the process of holococcolith formation occurs within vesicles (from now on referred to as “coccolith vesicle”) originating from the Golgi body (Figure 3), similar to the coccolith vesicle in heterococcolith forming cells.<sup>[3,33]</sup> These coccolith vesicles are strictly found at the cell periphery in proximity to the plasma membrane (Figure 3a,b,f). In contrast, cisternae containing organic scales are found in more proximal layers of the Golgi body

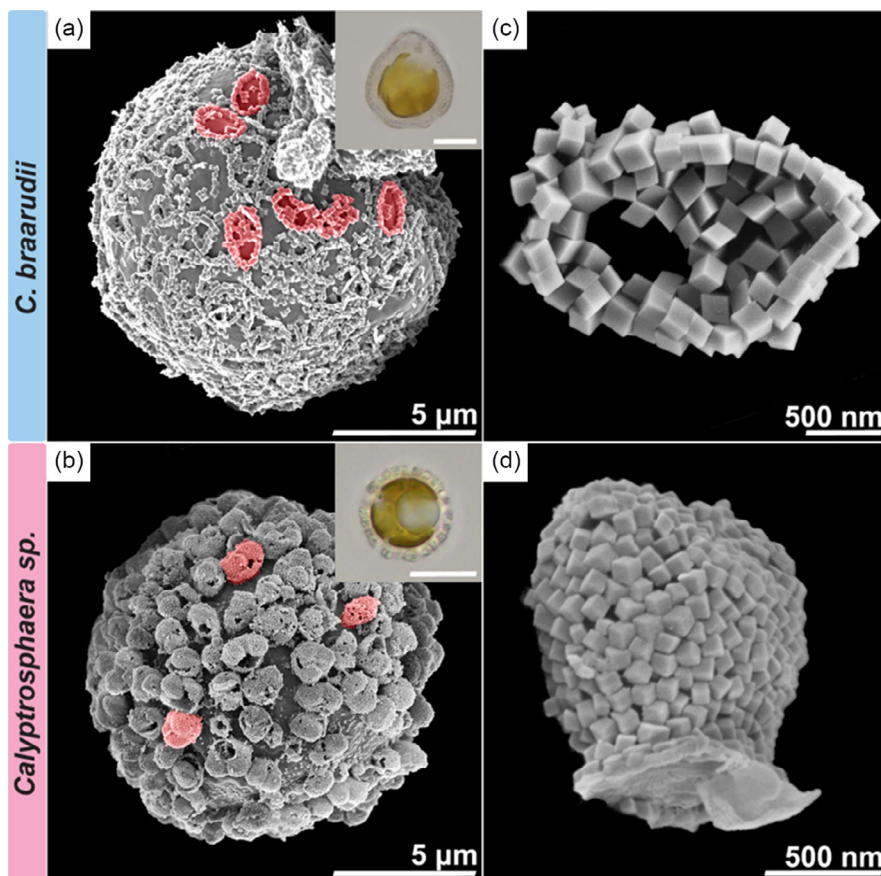


**Figure 1.** Holococcolith morphology in *C. braarudii* and *Calyptrosphaera* sp. a,b) Low-magnification SEM micrographs showing critical-point-dried cells fully covered by holococcoliths. Red pseudocoloring highlights single holococcoliths. Insets: light micrographs of single cells (holococcoliths are the hyaline layer covering the yellow-brown cell body). Scale bars in insets represent 10  $\mu\text{m}$ . c,d) Higher magnification SEM micrographs of single holococcoliths, showing the well-defined size of rhombohedral crystals assembled into species-specific ultrastructures. The base plate can be seen underlying the crystals of *Calyptrosphaera* sp. holococcolith.

(Figure 3a,b). Coccolith vesicles from both species are often observed near the flagellar pole of the cell (Figure S4, Supporting Information), a location reported by light microscopy as the site where new holococcoliths are extruded.<sup>[25,27]</sup>

In both species coccolith vesicles were found in two characteristic shapes, an elongated form (defined by an aspect ratio greater than 2), which resembles a Golgi cisterna (Figure 3c, S4d, Supporting Information), and a more ubiquitous subspherical form (an aspect ratio smaller than 2) (Figure 3, S4c, Supporting Information, see quantification in Figure S5, Supporting Information). The two vesicle morphologies were observed together in cells, with the elongated and thinner type at a proximal position, bringing the option that the two types may represent different developmental stages, whereby the elongated shape evolves into the spherical shape. The membrane of the coccolith vesicle could be seen in some sections engulfing a cytoplasmic pocket (Figure 3d, S5, Supporting Information), possibly providing a larger surface area for exchanging materials with the cytoplasm. Some coccolith vesicles contain an internal subvesicle enclosing many globular vesicles of  $\approx 50$  nm in diameter (cross sections in Figure 3b,e, surface view in Figure 3f, and

quantification in Figure S5, Supporting Information). It is possible that these subvesicles and the cytoplasmic pockets represent different planes of the same anatomical organization.

In many cases, several organic scales were observed within the coccolith vesicle, with a maximum of nine scales in spherical vesicles and two in elongated ones (Figure 3b,e,f, S5, Supporting Information). The multiple scales within the coccolith vesicle contrast with the single ones found in the more proximal Golgi cisternae, where scales are first seen. Within the larger spherical coccolith vesicles, scales were found at various orientations, even perpendicular to the Golgi cisternae (Figure 3e,f, S5, Supporting Information). The fusion of several Golgi cisternae into a single crystal-forming vesicle, or the continuous production of scales, could explain the observation of multiple scales and the large volume increase of the spherical vesicle.

### 2.3. Crystallization Mechanism of Holococcolith Crystals

In the heterococcolith developmental scheme, the growth pattern of the crystals is sequential. It starts with simultaneous and

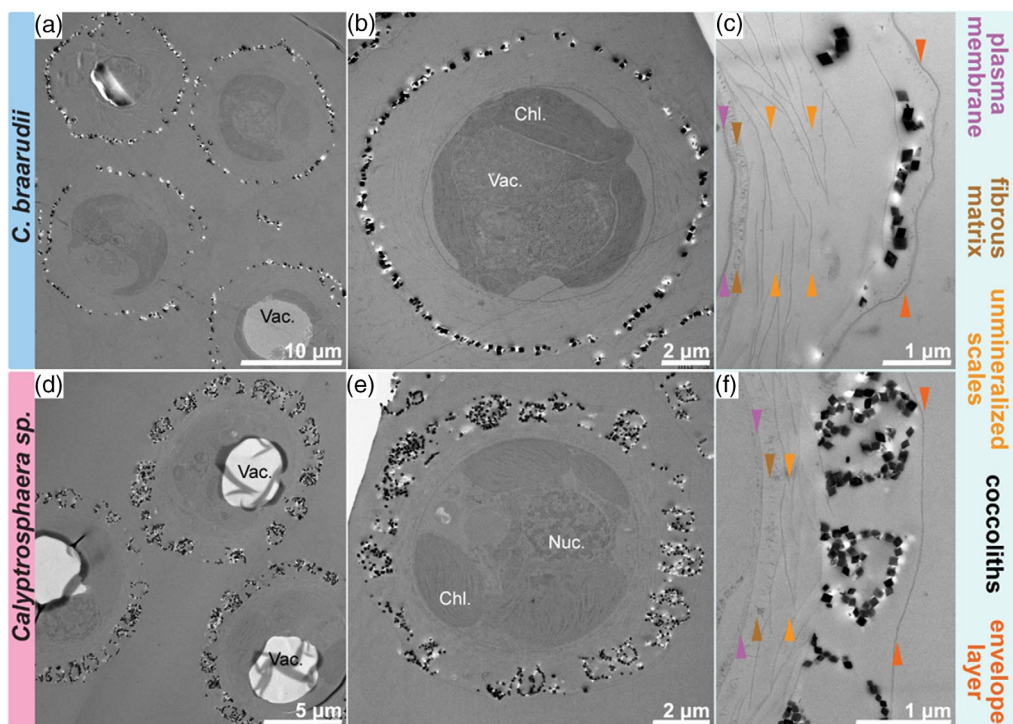


**Figure 2.** Intracellular and extracellular arrangement of holococcolith producing cells. a–f) TEM images of sectioned cells. Calcite crystals have dark contrast, while bright holes are visible where crystals have fallen out. a,d) Low- and b,e) high-magnification images showing cellular ultrastructure. Chl., chloroplast; Nuc., nucleus; Vac., vacuole. c,f) The various layers of the extracellular space are indicated with color-coded arrowheads according to the legend on the right.

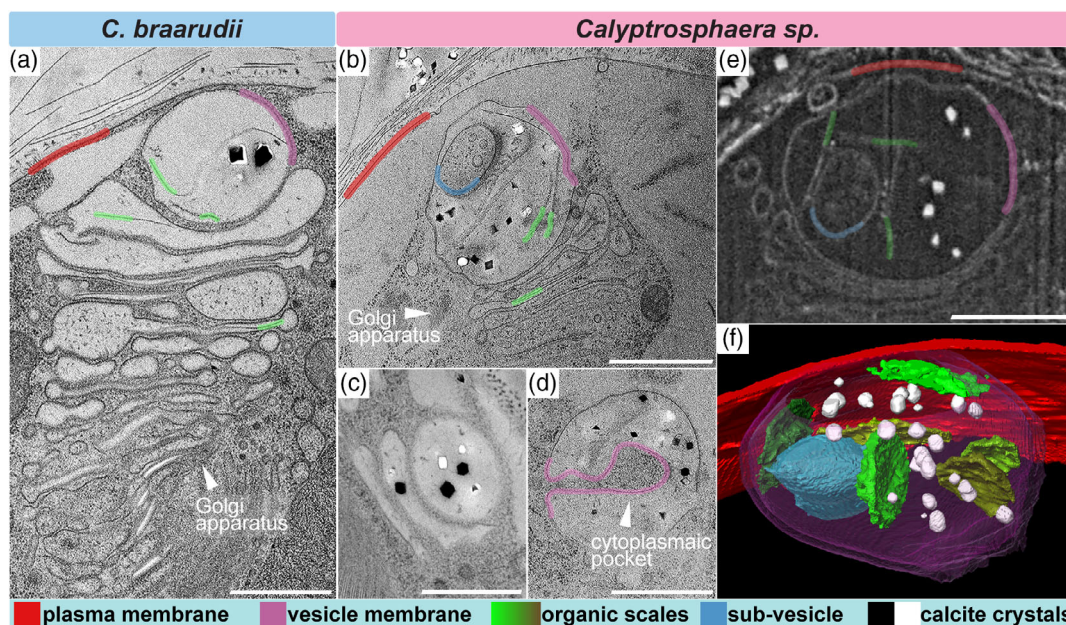


**Figure 3.** Intracellular morphology of holococcolith calcification. TEM images a–d) of HPF and freeze-substituted cells. a,b) Coccolith vesicles are part of the Golgi system, located in proximity to the plasma membrane. Organic scales are evident in both *cis*-Golgi cisternae and coccolith vesicles (partial false coloring). c) A section through a cell containing both elongated and spherical coccolith vesicles; the spherical vesicle is positioned more distally. d) A coccolith vesicle engulfing a pocket of cytoplasm. e) A single slice from the FIB-SEM dataset used for 3D visualization. f) A 3D visualization of a coccolith vesicle imaged by FIB-SEM volume imaging. Crystals are dispersed within the volume of the vesicle and are not adjacent to the organic scales. Scale bars represent 1  $\mu\text{m}$ . See also Movie S1, Supporting Information, for more details.

site-specific nucleation around the base plate, followed by synchronized growth of all crystals.<sup>[9]</sup> However, in contrast to the ordered nucleation pattern in heterococcoliths, our extensive TEM datasets and FIB-SEM data of an entire coccolith vesicle show that individual holococcolith crystals are dispersed within the coccolith vesicle space. Most crystals show no association with neighboring crystals or other organic structures detectable within the vesicle, such as the organic base plate scale, the sub-vesicle, and the coccolith vesicle membrane (Figure 3, Movie S1, Supporting Information).

In order to investigate possible patterns in the crystallization pathways of the holococcolith crystals we analyzed crystal sizes and numbers in the intracellular stages of coccolith formation. First, we measured the size of mature extracellular holococcolith crystals in TEM thin sections, using the maximum length of the rhombic diagonal (Figure 4a, red). The average size of these sectioned crystals was smaller than that of un-sectioned mature holococcoliths mounted directly on a TEM grid (Figure 4a, blue). This size reduction is because sectioning leaves only a fraction of the crystals, reducing the measured lengths in the sections. For example, in *Calyptrosphaera* sp. the sectioning effect reduces the average size of crystals from 120 nm (SD = 19 nm) in unsectioned mature holococcoliths, to 97 nm (SD = 23 nm) in sectioned mature holococcoliths. Nevertheless, sectioned intracellular crystals exhibited an even smaller average size of 79 nm (SD = 24) (Figure 4a, green), which arises only from

the fact that some intracellular crystals are in the midst of their growth process and are thus smaller than the mature extracellular crystals. A similar pattern was also found in *C. braarudii* (Figure 4b). It is important to note that crystal size varied considerably within a single vesicle, such that it was not common to find vesicles with uniformly small crystals, as observed for immature heterococcoliths. Even though this variability can originate as an artifact from sectioning, it is more likely the result of an unsynchronized crystal nucleation and growth process within vesicles.

A second trait that differentiates the synchronized nucleation of heterococcoliths from the situation in holococcoliths is the number of crystals within coccolith vesicles. In heterococcoliths, this number is constant from the early stages of coccolith formation and equals the number of crystals in mature coccoliths.<sup>[3,9,19,34]</sup> We compared crystal numbers in whole-mount mature holococcoliths, sectioned mature holococcoliths, and sectioned coccolith vesicles. For this analysis, which is affected to a greater extent by the sectioning plane relative to crystal size measurement, we used various sections (cross, median longitudinal, and lateral longitudinal sections) through mature holococcoliths. We found that the number of crystals within sectioned coccolith vesicles and in sectioned mature holococcoliths does not coincide, where fewer crystals are found in coccolith vesicles (Figure 4c,d). This difference strengthens the conclusion that nucleation is not a synchronized stage in holococcolith formation

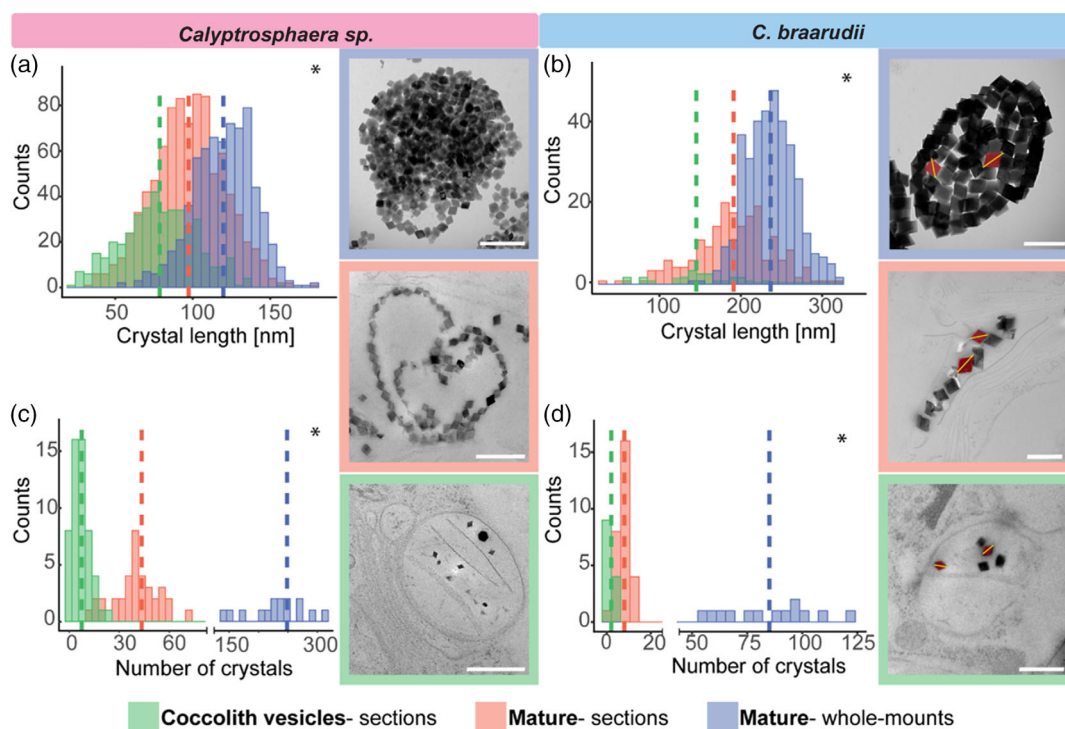


**Figure 4.** Sizes and numbers of crystals in developing and mature holococcoliths. a,b) Length measurements as a proxy for crystal sizes. Whole mounts of mature holococcoliths, sections of mature holococcoliths, and sections of coccolith vesicles are color coded. c,d) The number of crystals comprising each coccolith or coccolith vesicle from the same populations as in (a,b). The dashed lines indicate the average of each group. Representative TEM images from both species are shown in the same color code. Scale bars represent 500 nm. Length measurements are illustrated by yellow lines on red-colored crystals in *C. braarudii* images. Due to overlapping crystals in whole mounts of mature *Calyptrosphaera* sp., the data represent an underestimation of the actual numbers. In (a,b),  $*P < 0.05$ ; ANOVA followed by Tukey HSD. In (c,d),  $*Pr < 0.05$ ; Poisson regression model.

but occurs continuously and alongside crystal growth within a single coccolith vesicle.

### 3. Discussion

In this work, we show that the basic cellular process of coccolith formation, consisting of base plate formation and calcification within Golgi-derived vesicles, is similar in both life-cycle phases. However, in the haploid phase, coccoliths are not the outermost extracellular layer, as in the diploid phase, but are shielded from seawater by a thin organic envelope layer. In addition, the process of holococcolith crystallization is markedly different, with unsynchronized crystal nucleation and growth that is not directly regulated by insoluble macromolecules, such as the base plate and membranes. These similarities and differences are schematically summarized in **Figure 5**. An unresolved aspect is the absence of observations of coccolith vesicles containing fully assembled holococcolith ultrastructures, or similar crystal numbers as in the extracellular holococcoliths, which are both very common observations for heterococcoliths before secretion.<sup>[35]</sup> These final intracellular stages in which holococcoliths reach maturation may be missing from our dataset due to the possible rapid dynamics of the last stages of the process. Alternatively, part of holococcolith assembly may take place in an extracellular site. This latter scenario would require a morphogenetic mechanism fundamentally different from that of heterococcoliths.

Both holococcoliths and heterococcoliths exhibit tight cellular control over crystal size, morphology, and final orientation. However, they result in significantly different structures. The differences between the two formation schemes raise interesting questions about biomineral crystallization processes. From the

chemical point of view, holococcolith formation shares many more similarities with solution-mediated growth: unsynchronized nucleation, simple crystal habit, and a lumen without delimiting membranes. These properties can explain some of the differences between the two structures, such as the overall simpler shapes in holococcoliths. They can also direct us to possible important differences, such as the impact of confinement on crystal growth,<sup>[6,10,36]</sup> and the part of organic macromolecules in the crystallization process.

In heterococcoliths, the base plate is the exclusive site for nucleation, and once its periphery is fully mineralized, nucleation is exhausted. This notion is supported by the observation that the perimeter length of the base plate determines the number of nucleation events.<sup>[37]</sup> In contrast to the spatially and temporally regulated nucleation process of heterococcoliths, the random pattern in which intracellular holococcolith crystals are found and the disparity between the number of crystals found in coccolith vesicles and mature holococcoliths suggests that nucleation in holococcoliths is an unsynchronized process. In addition, most of the crystals within the holococcolith vesicle are not associated with the base plate, making stereochemical nucleation from the base plate unlikely. As the final number, size, and orientation of the crystals in holococcoliths are also controlled, these fundamental regulation processes may be independent of the base plate.

An important hallmark of heterococcolith biomineralization is the intricate crystal morphologies. Morphogenesis has been suggested to be mediated by two different factors. One is the tight interactions of growing crystals with vesicle membranes or neighboring crystals.<sup>[3]</sup> In this respect, the simple rhombohedral crystals of holococcoliths are in accordance with their

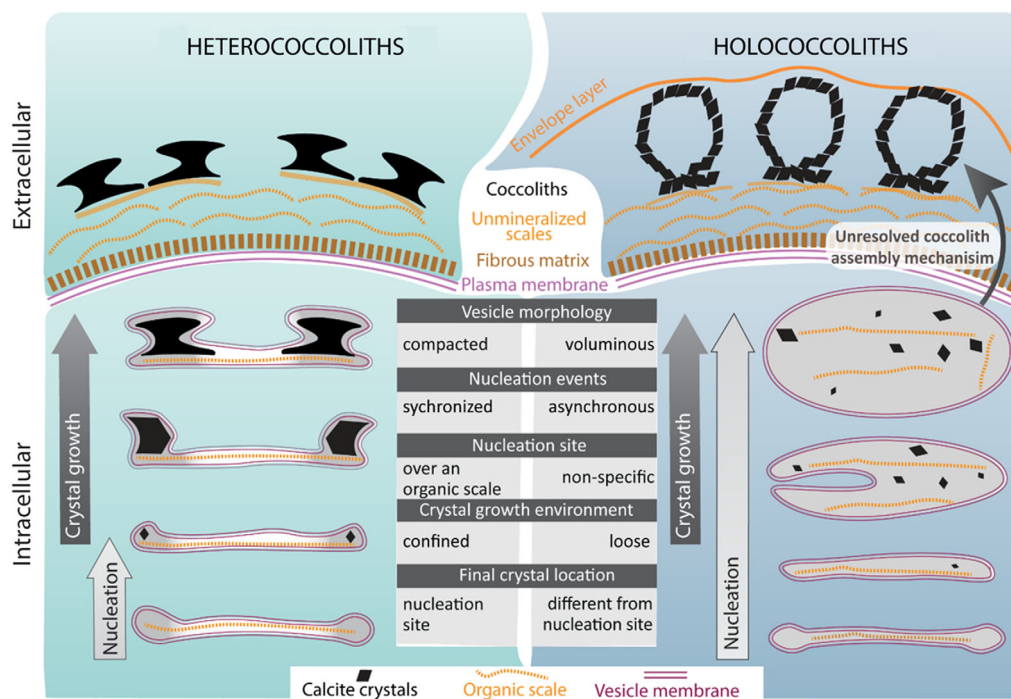


**Figure 5.** Schematic presentation of the calcification pathways of coccolithophore life-cycle stages. The known traits of heterococcolith formation are compared and contrasted with holococcolith characteristics that emerge from this study.

solution-like environment. The second factor is stereochemical modulations of crystal growth by specific binding of CAPs to crystal facets.<sup>[38]</sup> The fact that *Calyptrosphaera* sp. holococcolith crystals are covered by CAPs, like heterococcoliths, together with recent work showing the simple crystallographic habit of heterococcoliths,<sup>[3,10]</sup> suggests that the central role of CAPs is not as crystal growth modifiers by binding to crystal facets. It is plausible that the main function of CAPs is related to the transport of calcium ions to the site of precipitation and dictating calcite nucleation.<sup>[3,14,20,39]</sup>

One of the most intriguing aspects of holococcolith biomineralization, which is not addressed by this study, is the assembly process of the rhombohedral calcite into the complex and species-specific superstructures. Ultrastructure could be achieved by templating crystal nucleation, controlling both location and orientation of the crystals, as in the heterococcolith formation pathway, or by packing fully grown crystals nucleated at random sites. We could not detect any substance templating crystal nucleation; however, this can be a limitation of the sample preparation and imaging techniques used. Future work using cryoelectron microscopy techniques may reveal more information about this enigmatic process.

## 4. Conclusion

In this work, we identify basic aspects of the holococcolith crystal nucleation and growth environment, and compare it to the widely studied heterococcoliths. The calcification compartment of holococcoliths is a relatively unconfined space, giving rise to simple rhombohedral crystals, yet of defined sizes and architecture. As both holococcoliths and heterococcoliths are the result of regulated biological crystallization, the differences reported here spotlight the nanoenvironment in which crystals grow in terms of the roles of confinement and functional macromolecules modulators of the crystallization process. Future research is needed to elucidate the mechanism of packing the rhombohedral crystals into the elaborate holococcoliths ultrastructures.

## 5. Experimental Section

**Cell Cultures:** Clonal cultures of *C. braarudii* (RCC3777) and *Calyptrosphaera* sp. (RCC1181) obtained from the Roscoff Culture Collection (www.roscoff-culture-collection.org) were grown in sterile-filtered seawater collected from the Mediterranean Sea, with salinity corrected to 35 psu. Additional supplements were aseptically added according to the K/2 nutrient recipe.<sup>[40]</sup> Culturing was conducted in a temperature-controlled culture room at 18 °C with illumination provided by LED lights at an intensity of 10–20  $\mu\text{mol m}^{-2} \text{s}^{-1}$  under a 16:8 light:dark cycle. Inoculation of 2 week-old cultures (density of  $\approx 7.5 \times 10^5$  cell  $\text{mL}^{-1}$  for *Calyptrosphaera* sp. and  $\approx 2.5 \times 10^5$  for *C. braarudii*) was undertaken by a dilution factor of 1:10 into fresh seawater media.

**Decalcification and Recalcification:** To maximize the chance of observing intracellular stages of holococcolith calcification by TEM, we enriched the proportion of calcifying cells in the culture. As decalcification of extracellular coccoliths has been shown to induce coccolith production in heterococcoliths,<sup>[41]</sup> we attempted to apply a similar decalcification method for holococcoliths. However, ethylenediaminetetraacetic acid (EDTA)-based decalcification was found to be unsuitable for the studied species because it resulted in the formation of large aggregates upon

removal of residual EDTA. The chosen method was acidifying and subsequently neutralizing the culture media, eliminating the need for washes with centrifugation. 50 mL of an exponential phase culture of  $\approx 10^5$  cell  $\text{mL}^{-1}$  were acid-decalcified by lowering the medium pH to 5 using 1 M HCl. Once pH = 5 was reached, 1 M NaOH was added to restore the pH to 8.2. During this process, the culture was stirred by a magnetic stirrer, and the pH was monitored with a pH meter. Cells were left to recalcify for 12 h; the time point at which the coccolith production rate was highest (Figure S1B, Supporting Information). The decalcification treatment was coupled with the onset of the daylight phase to ensure reproducible results.

**SEM:** To avoid the crushing of the cellular structure associated with the surface tension of water, samples for SEM were dehydrated in increasing concentration of ethanol (30%, 70%, and 100%), followed by critical-point drying using the BAL-TEC CPD 030 instrument equipped with a small particle holder suited for particles in the range of 2–30  $\mu\text{m}$  (Tousimis Research Corporation). Once dried, powder of cells were mounted on an aluminum stub (EMS 75230) and sputter-coated with 2.5 nm of iridium. Scanning electron micrographs were produced with a Zeiss Ultra 55 microscope, using 2 kV acceleration voltage and an InLens detector.

**Light Microscopy:** Light microscopy investigations were carried out using a Nikon Eclipse Ni-U upright microscope. 30  $\mu\text{L}$  of culture were mounted on a glass microscope slide and topped with a cover slide. Images were captured using the paired camera with NIS Elements v 5.02 imaging software (Nikon Corporate, Tokyo, Japan).

**Ruthenium Red Staining:** Ruthenium red (Sigma, 00541-1G) was dissolved in seawater media until saturation. The dye solution was added to a cell culture or isolated holococcoliths at a 1:1 volume ratio and was incubated overnight with continuous agitation. Cells/coccoliths were then washed by centrifugation 3 times with fresh seawater.

**HPF:** Exponentially growing cultures were gently concentrated by settling in a conical tube for 2 h in growth room conditions. For the calcification studies, recalcifying cultures were concentrated by gentle centrifugation (500 g, 5 min). The dense culture suspension was loaded into a 100  $\mu\text{m}$  deep aluminum HPF disc and covered with an aluminum cap. The sample was then vitrified at liquid nitrogen temperature at 210 MPa using a HPF machine (Leica Microsystems GmbH).

**Freeze Substitution and Epon Embedding:** High-pressure frozen samples were transferred into a freeze-substitution device (EM AFS2, Leica Microsystems GmbH) precooled to  $-90$  °C. Samples were then immersed in an anhydrous acetone solution containing the following combination of fixatives and stains: 0.2% uranyl acetate (UA), 0.2% osmium tetroxide ( $\text{OsO}_4$ ), and 2% glutaraldehyde (GA). Heating from  $-90$  °C to room temperature was conducted using the following sequence: 48 h at  $-90$  °C, linear rise during 24 h to  $-20$  °C, and a 1 h linear rise to 0 °C. At 0 °C, samples were taken out of the FS Dewar and brought to room temperature. Embedding in Epon (Polysciences Europe GmbH, Germany) was conducted using a gradient concentration mixture (10%, 20%, 30%, 40%, 60%, 80%, 100% Epon in acetone) at room temperature. Epon-embedded samples were cured at 60 °C for 72 h.

**Chemical Fixation:** Cells were pelleted by gentle centrifugation (500 g, 5 min) and resuspended in 1 mL of fixation buffer (4% paraformaldehyde [PFA] and 2% GA in artificial sea water). Fixation was conducted under mild shaking conditions at room temperature for 2 h. The pellets were then embedded in agar (Noble, Sigma-Aldrich Corporate, St. Louis, USA) made with artificial seawater. Pellets in agar were postfixed in a solution containing 1%  $\text{OsO}_4$ , 0.5% potassium dichromate ( $\text{K}_2\text{Cr}_2\text{O}_7$ ), and 0.5% potassium hexacyanoferrate ( $\text{K}_4[\text{Fe}(\text{CN})_6]$ ). After washing, samples were stained with 2% UA for 1 h. The pellet was then dehydrated in graded ethanol/artificial seawater solutions, followed by Epon embedding (Polysciences Europe GmbH, Germany) through a series of solution substitutions, and cured at 60 °C for 72 h.

**Sectioning:** Epon-embedded samples were sectioned to a thickness of 70 nm using Leica Ultracut UCT ultramicrotome (Leica Microsystems GmbH) equipped with an Ultra 45° diamond knife (Diatome Ltd., Nidau, Switzerland). As the calcite crystals of interest readily dissolve in distilled water, sectioning was carried out over a bath of 99.8%

anhydrous ethylene glycol (Sigma–Aldrich Corporate, St. Louis, USA), in which calcite is insoluble.<sup>[31]</sup> Sections were mounted on copper TEM grids with a carbon support film.

**TEM:** Ultrathin sections were imaged with an FEI Tecnai Spirit transmission electron microscope (FEI, Eindhoven, The Netherlands) operated at 120 kV and equipped with a Gatan Oneview camera.

**FIB-SEM:** For FIB-SEM, *Calyptosphaera* sp. samples were prepared by the HPF-FS and embedded in Epon as described above. FIB-SEM images acquisition was performed on a Crossbeam 550 FIB-SEM (Carl Zeiss Vision GmbH). Specimens were coated with a conductive layer of iridium (10 nm), prepared with sputter coating CCU-010 HV (Safematic). Prior the acquisition, a wide trench of about 80 μm was milled using ion beam of 30 nA, 30 kV, in order to expose a big area of the sample. Once the region of interest was defined on the cross-sectional face, the ion beam current was reduced to 700 pA, and slicing process was performed with Serial Surface Imaging algorithm of SmartFIB SW (Zeiss). SEM images were acquired at 1.6 kV, 350 pA, with InLens detector and noise reduction of line averaging ( $n = 120$ ). Image series of consecutive sections were collected using an voxel size of  $7.6 \times 7.6 \times 9$  nm. Image processing and images stack alignment were performed by Fiji image processing package (National Institutes of Health, Bethesda, MD, USA). 3D reconstruction was prepared in Amira-Avizo (Thermo Fisher Scientific). Segmentation of 3D volumes was conducted manually using Amira-Avizo. A membrane enhancement filter was used to assist with the segmentation of membranes.

**Crystal Length and Number Measurements:** Measurements of the rhombic crystals were conducted on both sectioned and whole-mount samples. The length of the largest diagonal, which was used to indicate overall crystal size, was measured. Measurements were conducted manually using ImageJ. ANOVA, Tukey HSD, and Poisson regression statistical analysis were performed using the “gl” package for RStudio.

## Supporting Information

Supporting Information is available from the Wiley Online Library or from the author.

## Acknowledgements

This research was supported by the Israel Science Foundation (grant no. 697/19).

## Conflict of Interest

The authors declare no conflict of interest.

## Data Availability Statement

The data that support the findings of this study are available in the supplementary material of this article.

## Keywords

biomineralization, calcites, coccoliths, crystal growths, haploid–diploid life cycles

Received: December 6, 2022  
Published online: January 10, 2023

[1] H. A. Lowenstam, S. Weiner, *On Biomineralization*, Oxford Univ. Press, New York 1989.

- [2] S. Mann, *Biomineralization: Principles and Concepts in Bioinorganic Materials Chemistry*, Oxford Univ. Press, New York 2001.
- [3] Y. Kadan, F. Tollervey, N. Varsano, J. Mahamid, A. Gal, *Proc. Natl. Acad. Sci. U.S.A.* **2021**, *118*, 46.
- [4] C. Heintze, P. Formanek, D. Pohl, J. Hauptstein, B. Rellinghaus, N. Kröger, *BMC Mater.* **2020**, *2*, <https://doi.org/10.1186/s42833-020-00017-8>.
- [5] R. Uebe, D. Schüler, *Nat. Rev. Microbiol.* **2016**, *14*, 621.
- [6] F. C. Meldrum, C. O’Shaughnessy, *Adv. Mater.* **2020**, *32*, 2001068.
- [7] M. Grzelczak, J. Vermant, E. M. Furst, L. M. Liz-Marzán, *ACS Nano* **2010**, *4*, 3591.
- [8] J. R. Young, K. Henriksen, *Rev. Mineral. Geochem.* **2003**, *54*, 189.
- [9] J. R. Young, J. M. Didymus, P. R. Brown, B. Prins, S. Mann, *Nature* **1992**, *356*, 516.
- [10] E. M. Avrahami, L. Houben, L. Aram, A. Gal, *Science* **2022**, *376*, 312.
- [11] A. Houdan, C. Billard, D. Marie, F. Not, A. G. Sâez, J. R. Young, I. Probert, *Syst. Biodivers.* **2004**, *1*, 453.
- [12] M. J. Frada, E. M. Bendif, S. Keuter, I. Probert, *Perspect. Phycol.* **2019**, *6*, 11.
- [13] A. Gal, R. Wirth, J. Kopka, P. Fratzl, D. Faivre, A. Scheffel, *Science* **2016**, *353*, 590.
- [14] M. E. Marsh, *Protoplasma* **1999**, *207*, 54.
- [15] K. M. Wilbur, N. Watabe, *Ann. N. Y. Acad. Sci.* **1963**, *109*, 82.
- [16] D. E. Outka, D. C. Williams, *J. Protozool.* **1971**, *18*, 285.
- [17] Z. Eyal, L. Krounbi, O. Ben Joseph, E. M. Avrahami, I. Pinkas, H. Peled-Zehavi, A. Gal, *Acta Biomater.* **2022**, *148*, 336.
- [18] P. Westbroek, E. W. De Jong, P. Van Der Wal, A. H. Borman, J. P. M. De Vrind, D. Kok, W. C. De Bruijn, S. B. Parker, *Philos. Trans. R. Soc. London. B, Biol. Sci.* **1984**, *304*, <https://doi.org/10.1098/rstb.1984.0037>.
- [19] J. M. Walker, B. Marzec, N. Ozaki, D. Clare, F. Nudelman, *J. Struct. Biol.* **2020**, *210*, 107476.
- [20] M. E. Marsh, *Protoplasma* **1994**, *177*, 108.
- [21] A. H. Borman, W. E. de Vrind-de Jong, D. J. Kok, P. Westbroek, L. Bosch, *Eur. J. Biochem.* **1982**, *129*, 179.
- [22] L. Addadi, Z. Berkovitch Yellin, N. Domb, E. Gati, M. Lahav, L. Leiserowitz, *Nature* **1982**, *296*, 21.
- [23] D. B. DeOliveira, R. A. Laursen, *J. Am. Chem. Soc.* **1997**, *119*, 10627.
- [24] I. Manton, G. F. Leedale, *Arch. Mikrobiol.* **1963**, *47*, 115.
- [25] J. D. Rowson, B. S. C. Leadbeater, J. C. Green, *Br. Phycol. J.* **1986**, *21*, 359.
- [26] D. Klaveness, *Nord. J. Bot.* **1973**, *20*, 151.
- [27] G. Langer, A. R. Taylor, C. E. Walker, E. M. Meyer, O. Ben Joseph, A. Gal, G. M. Harper, I. Probert, C. Brownlee, G. L. Wheeler, *New Phytol.* **2021**, *231*, 1845.
- [28] I. Probert, A. Houdan, in *Coccolithophores From Molecular Processes to Global Impact* (Eds.: H. R. Thierstein, J. R. Young), Springer, Berlin, Heidelberg **2004**, pp. 217–249.
- [29] D. Studer, M. Muller, M. Michel, in *High pressure freezing comes of age*, Scanning Microsc. Supplement 3, AMF O’Hare International, Chicago **1989**, pp. 253–269.
- [30] R. A. Steinbrecht, M. Müller, in *Cryotechniques in Biological Electron Microscopy* Springer, Berlin Heidelberg, **1987**, pp. 149–172.
- [31] Y. Kadan, L. Aram, E. Shimoni, S. Levin-Zaidman, S. Rosenwasser, A. Gal, *J. Struct. Biol.* **2020**, *210*, 107465.
- [32] S. Sviben, A. Gal, M. A. Hood, L. Bertinetti, Y. Politi, M. Bennet, P. Krishnamoorthy, A. Schertel, R. Wirth, A. Sorrentino, E. Pereiro, D. Faivre, A. Scheffel, *Nat. Commun.* **2016**, *7*.
- [33] P. van der Wal, L. de Jong, P. Westbroek, W. C. de Bruijn, *Ecol. Bull.* **1983**, *251*.
- [34] J. M. Didymus, J. R. Young, S. Mann, *Proc. R. Soc. London. Ser. B Biol. Sci.* **1994**, *258*, 237.



- [35] X. Yin, A. Ziegler, K. Kelm, R. Hoffmann, P. Watermeyer, P. Alexa, C. Villinger, U. Rupp, L. Schlüter, T. B. H. Reusch, E. Griesshaber, P. Walther, W. W. Schmahl, *J. Phycol.* **2018**, *54*, 85.
- [36] A. S. Finomore, M. R. J. Scherer, R. Langford, S. Mahajan, S. Ludwigs, F. C. Meldrum, U. Steiner, *Adv. Mater.* **2009**, *21*, 3928.
- [37] T. Beuvier, I. Probert, L. Beaufort, B. Suchéras-Marx, Y. Chushkin, F. Zontone, A. Gibaud, *Nat. Commun.* **2019**, *10*, <https://doi.org/10.1038/s41467-019-08635-x>.
- [38] K. Henriksen, S. L. S. Stipp, J. R. Young, M. E. Marsh, *Am. Mineral.* **2004**, *89*, 1709.
- [39] A. J. Giuffre, L. M. Hamm, N. Han, J. J. De Yoreo, P. M. Dove, *Proc. Natl. Acad. Sci. U.S.A.* **2013**, *110*, 9261.
- [40] M. D. Keller, R. C. Selvin, W. Claus, R. R. L. Guillard, *J. Phycol.* **1987**, *23*, 633.
- [41] P. van der Wal, J. P. M. de Vrind, E. W. de Vrind-de Jong, A. H. Borman, *J. Phycol.* **1987**, *23*, 218.